J. Fluid Mech. (1996), vol. 317, pp. 91–109

Rendering a subcritical Hopf bifurcation supercritical

By PO KI YUEN AND HAIM H. BAU[†]
Department of Mechanical Engineering and Applied Mechanics, University of Pennsylvania, Philadelphia, PA, 19104-6315, USA

(Received 8 August 1995 and in revised form 18 January 1996)

It is demonstrated experimentally and theoretically that through the use of a nonlinear feedback controller, one can render a subcritical Hopf bifurcation supercritical and thus dramatically modify the nature of the flow in a thermal convection loop heated from below and cooled from above. In particular, we show that the controller can replace the naturally occurring chaotic motion with a stable, periodic limit cycle. The control strategy consists of sensing the deviation of fluid temperatures from desired values at a number of locations inside the loop and then altering the wall heating to counteract such deviations.

1. Introduction

In many industrial processes and in propulsion it is often desirable to maintain flow conditions other than the naturally occurring ones. For example, if at high Reynolds numbers, one were able to maintain laminar flow instead of the naturally occurring turbulent flow, one would be able to reduce drag and fuel cost. Recently, Hu & Bau (1994) have demonstrated that through the use of a linear feedback controller, it is possible to significantly delay the linear loss of stability of planar Poiseuille flows. Unfortunately, the loss of stability of the planar Poiseuille flow occurs through a subcritical Hopf bifurcation (Chen & Joseph 1973). This bifurcation is likely to remain subcritical in the presence of a linear controller. As a result, both the controlled and uncontrolled laminar Poiseuille states may have a limited basin of attraction. In other words, in practice, the transition to turbulence occurs at much smaller Reynolds numbers than those predicted by linear stability theory. A similar situation exists in many other important flow systems.

This early transition would be less likely to occur if the bifurcation at the point of linear loss of stability were supercritical. Abed & Fu (1986) proposed the use of nonlinear feedback control to invert the direction of the bifurcation. Until now, the feasibility of this idea has not been verified in experiments. Our objective is to demonstrate experimentally and theoretically that through the use of a nonlinear feedback controller it is possible to render a subcritical bifurcation supercritical and thereby potentially increase the domain of attraction of the stable subcritical state.

We chose to study a relatively simple convective system, the thermal convection loop, because it exhibits rich dynamics ranging from no motion through steady motion to chaos and yet it can be analysed, at least qualitatively, using a low-dimensional dynamical model and the theoretical predictions can be readily tested by simple experiments. Moreover, even though this system is a relatively simple one, it is,

---

[†] All correspondence should be directed to this author.

nonetheless, important since thermal convection loops provide a means for circulating fluid without the use of pumps. Such loops are of interest for solar heaters, emergency reactor-core cooling, and process industries. They also are of interest for understanding warm springs, sea water circulation in the oceanic crust, and formation of ore deposits. Singer, Wang & Bau (1991), Singer & Bau (1991), and Wang, Singer & Bau (1992, hereafter referred to as WSB) used a similar thermal convection loop to demonstrate that linear feedback control strategies can be effective in modifying the bifurcation structure of the flow in the loop and in delaying or advancing the transition to chaos. Many of the ideas which emerged from the aforementioned studies were later implemented in more complex flow systems such as Rayleigh–Bénard convection (Tang & Bau 1993*a*, *b*, 1994).

2. Theoretical study

In this section, we set forth a simple mathematical model for the flow in the loop, summarize briefly the solutions of the governing equations for the uncontrolled system, modify these equations to include a nonlinear feedback controller, and analyse the controlled system.

2.1. *The governing equations*

Consider a thermal convection loop constructed from a pipe bent into a torus and standing in the vertical plane as depicted in figure 1. The diameter of the pipe is d, and the diameter of the torus is D. θ is the angular location of a point on the torus. The wall temperature of the pipe, $T_w(\theta, t)$, which may vary both with the angular location θ and time t, is symmetric with respect to the torus axis that is parallel to the gravity vector. Variations in the wall temperature may cause a spatial temperature distribution inside the fluid which, under appropriate conditions, may induce fluid motion in the loop.

We analyse the motion in the loop within the framework of Boussinesq's approximation, using a one-dimensional model consisting of mass, momentum and energy balances (Bau & Torrance 1980; WSB):

$$u = u(t), \tag{1}$$

$$\dot{u} = \frac{1}{\pi} Ra\, P \oint T \cos(\theta)\, \mathrm{d}\theta - Pu, \tag{2}$$

and

$$\dot{T} = -u\frac{\partial T}{\partial \theta} + B\frac{\partial^2 T}{\partial \theta^2} + [T_w(\theta, t) - T]. \tag{3}$$

The fluid is assumed to be incompressible and Newtonian. In the above, all quantities are non-dimensional; $Ra = g\beta\Delta T\tau^2/(DP)$ is the loop's Rayleigh number; β is the thermal expansion coefficient; g is the gravitational acceleration; and ΔT is the averaged wall temperature difference between the loop's bottom and top. The timescale is $\tau = \rho_0 C_P d/(4h)$, where ρ_0 is the fluid's average density, C_P is the thermal capacity, and h (which we assume to be constant) is the heat transfer coefficient between the fluid and the pipe's wall. $P = 32\nu\tau/d^2 = 8Pr/Nu$ is the loop's Prandtl number, where ν is the kinematic viscosity. $Pr = \nu/\alpha$ and $Nu = hd/\kappa$ are the conventional Prandtl and Nusselt numbers, respectively. α and κ are, respectively, the fluids thermal diffusivity and conductivity; and $B = (d/D)^2/Nu$ is the Biot number. The lengthscale is the torus radius, $D/2$. The various approximations leading to equations (1)–(3) were detailed in WSB.

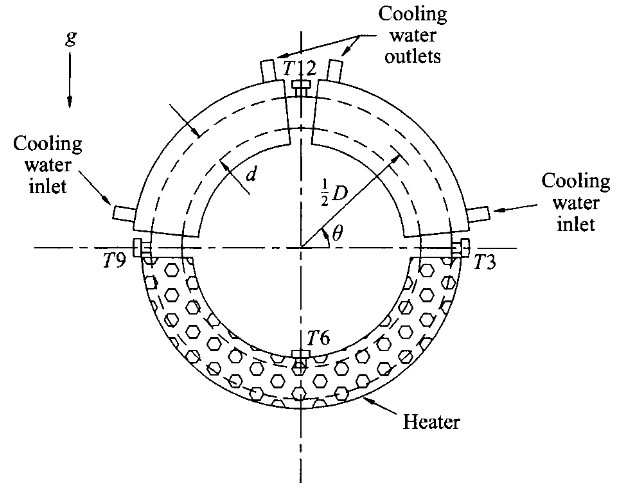

FIGURE 1. Schematic description of the experimental apparatus.

The flow dynamics in the uncontrolled loop have been investigated by, among others, Gorman, Widmann & Robins (1984, 1986), Widmann, Gorman & Robins (1989), Hart (1984, 1985), Yorke, Yorke & Mallet-Paret (1987), and Ehrhard & Muller (1990). By expanding the fluid and wall temperatures into Fourier series, substituting the series into equations (1)–(3) and requiring the equations to be satisfied in the sense of weighted residuals, one obtains an infinite set of ordinary differential equations. Three of the equations decouple from the rest of the set (with exact closure) and can be solved independently of the other equations without the need of truncation (Malkus 1972; WSB). These three equations describe the invariant manifold of the system. One can obtain a description of the flow dynamics by solving the equations

$$\dot{u} = P(c-u), \tag{4}$$

$$\dot{c} = -us-c, \tag{5}$$

and

$$\dot{s} = uc-s+RaW_1. \tag{6}$$

Roughly speaking, the variables $c(t)$ and $s(t)$ are proportional, respectively, to the fluid's temperature differences between positions 3 and 9 o'clock and positions 12 and 6 o'clock around the loop. These are the variables we will measure in our experiments. Below, we use $P = 4$ since this value approximates the loop's Prandtl number in our experimental apparatus. In the absence of control, $W = -1$ and equations (4)–(6) are the celebrated Lorenz equations (1963).

2.2. *The uncontrolled flow – a summary*

Equations (4)–(6) with $W_1 = -1$ have been investigated exhaustively in the literature (i.e. Robbins 1977; Sparrow 1982; Bau & Wang 1991). Here, we summarize very briefly some details relevant to our present study. Equations (4)–(6) with $W_1 = -1$ possess a number of equilibrium states, such as

(i) a no-motion state (B_0: $u = c = 0$, $s = -Ra$) which is both globally and linearly stable for $Ra < 1$ and linearly non-stable for $Ra > 1$;

(ii) time-independent motion either in the clockwise (B_-) or counterclockwise (B_+) direction ($B_\pm : u = c = \pm\bar{c}, s = -1$), where $\bar{c} = (Ra-1)^{1/2}$. $B_\pm$ are linearly stable for $1 < Ra < Ra_H = 16$; and

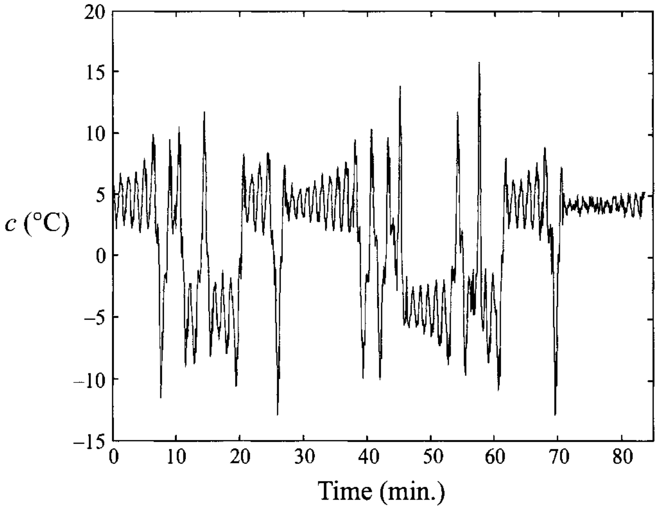

FIGURE 2. The experimentally measured temperature difference between positions 3 and 9 o'clock is depicted as a function of time for $Q = 330$ W $= 3.3Q_C$.

(iii) chaotic motion (B_C) for $Ra > Ra_H$ with occasional windows of periodic behaviour. In the chaotic regime, the motion in the loop consists of irregular oscillations with occasional reversals in the direction of the flow. For example, for $Ra \sim 3.3Ra_H$, figure 2 depicts the experimentally observed temperature difference, $c \sim \Delta T_{3-9}$, between positions 3 and 9 o'clock as a function of time. The positive and negative values of c correspond to flow in the counterclockwise and clockwise directions, respectively. Qualitatively similar behaviour was obtained in numerical simulations.

At $Ra = Ra_H = 16$, the $B_\pm$ states lose stability via a subcritical Hopf bifurcation. The resulting periodic orbit, B_P, is non-stable and its period increases as Ra decreases. At $Ra = Ra_{hom}$, B_P becomes a homoclinic orbit and it passes through the no-motion state, B_0. At $Ra = Ra_{hom}$, there is a bifurcation, the homoclinic explosion, which results in an assortment of non-stable periodic and non-periodic orbits, known collectively as the non-wandering set, which is initially non-attracting. As Ra increases above Ra_{hom}, at $Ra = Ra_A < Ra_H$, the non-wandering set becomes an attractor. The coexistence of a number of attractors in the interval between Ra_A and Ra_H gives rise to a hysteresis phenomenon. When one starts an experiment at $Ra < Ra_H$ and gradually increases Ra, the transition from $B_\pm$ to B_C occurs at $Ra = Ra_H$. When, however, one starts an experiment in which initially $Ra > Ra_H$ and gradually decreases Ra, the transition from B_C to $B_\pm$ occurs at $Ra = Ra_A < Ra_H$. Since in our loop ($P = 4$), $Ra_A \sim 15.984$, the interval between Ra_A and Ra_H is very small and it may not be possible to detect the hysteresis phenomenon in experiments.

2.3. *Active control of the flow*

WSB used linear feedback control to stabilize (increase Ra_H) and destabilize (decrease Ra_H) the time-independent state (B_+). In other words, WSB obtained (i) steady, non-oscillatory flow under conditions in which the uncontrolled flow is nominally chaotic without significantly changing the operating conditions and the structure of the loop; and (ii) chaotic flow under conditions for which the uncontrolled flow is nominally time-independent.

In the uncontrolled system, the Hopf bifurcation occurring at $Ra = Ra_H$ is subcritical and it remains subcritical when the linear controller is used to increase Ra_H. Since the subcritical bifurcating periodic orbit is non-stable, it would never be observed in an experiment. When one conducts an experiment in which Ra is gradually increased, once Ra exceeds Ra_H the bifurcation diagram undergoes an abrupt change from time-independent to chaotic flow. Our objective is to use nonlinear control to render the subcritical bifurcation supercritical. The objective of the nonlinear controller is to assure a smooth transition from B_+ to B_P at Ra_H. The nonlinear controller itself does not affect the magnitude of Ra_H.

In our experiments, we measured the temperature differences $c(t)$ and $-s(t)$ between positions 3 and 9 o'clock and between positions 6 and 12 o'clock around the loop as functions of time and we controlled the heat input to the heater. In our mathematical model, we control the wall temperature which is proportional to the heat input. The nonlinear control law is

$$W_1 = -1 - \frac{k_p}{Ra}[c(t) - \bar{c}] - \frac{k_n}{Ra} f(c(t) - \bar{c}), \tag{7}$$

where k_p and k_n are, respectively, the linear (proportional) and nonlinear control gains. $f(\chi)$ is a nonlinear function with $f(0) = f'(0) = 0$. In the discussion below, we used the controller $f(\chi) = \chi^3$.

The state we wish to stabilize, $\{B_+ : u = c = \bar{c}, s = -1\}$, is an equilibrium state of both the controlled and uncontrolled systems. In other words, the controller (7) affects the system's dynamics but does not alter the equilibrium state, B_+. WSB shows that Ra_H increases as k_p decreases. The nonlinear controller has no effect on this linear stability of B_+.

Although the controller does not alter B_+, it does alter the other equilibrium states of the system. The no-motion state in the controlled system is $\{B_0$: $u = c = 0$, $s = -1 + \bar{c}[k_p + \bar{c}(k_n \bar{c} - 1)]\}$. The uncontrolled, clockwise-motion state is replaced in the controlled system with the two states

$$\left\{ B^{\pm}_{-} : u = c = \bar{c} + \frac{1}{2k_n}(1 \pm (1 - 4k_n k_p + 8k_n \bar{c})^{1/2}), s = -1 \right\}.$$

The branches ($B^{\pm}_{-}$) exist only when $Ra > 1$ and $(8k_n \bar{c} > 4k_n k_p - 1)$. Depending on the magnitude of the various parameters, $B^{\pm}_{-}$ may represent either clockwise or counterclockwise flows. The stability characteristics of B_0 and $B^{\pm}_{-}$ are discussed in Yuen (1997). For example, figure 3 depicts c as a function of Ra for $k_p = -2$ and $k_n = -0.1$. The solid and dashed lines in figure 3 correspond, respectively, to linearly stable and non-stable states.

The nonlinear controller $f(\chi) = \chi^3$ has one unfortunate feature. While the uncontrolled system is bounded in the sense that no matter what the initial conditions are, trajectories will eventually enter an ellipsoid in phase space (Sparrow 1982), the same may not be true for the controlled system. In the latter case, the possibility that certain initial conditions may lead to trajectories diverging to infinity cannot be excluded. In practice, the actuator's saturation will prevent such a divergence from occurring. Alternatively, in order to avoid potentially diverging behaviour, one can choose a bounded function such as $f(\chi) = -3(\tanh(\chi) - \chi)$ to effect the nonlinear control. This nonlinear controller leads to very similar results to the one presented below for the cubic controller.

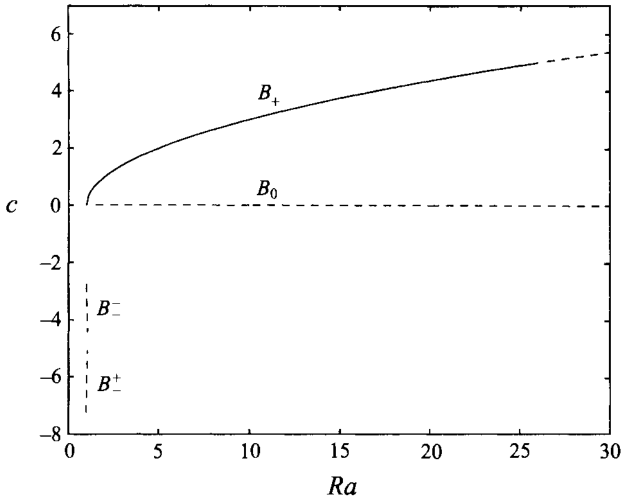

FIGURE 3. The time-independent solutions of the controlled system. $P = 4$, $k_p = -2$, $k_n = -0.1$. The solid and dashed lines correspond, respectively, to linearly stable and nonstable solutions.

2.4. *Weakly nonlinear analysis*

In order to investigate the nature of the periodic solution which bifurcates from B_+ at $Ra = Ra_H$, we carried out a weakly nonlinear analysis. x_1, x_2, and x_3 denote, respectively, the deviations of u, c, and s from B_+. $\boldsymbol{x} = \{x_1, x_2, x_3\}$. Equations (4)–(7) rewritten in local form are

$$\mathrm{L}_1(Ra)\,\boldsymbol{x} = \dot{\boldsymbol{x}} + \mathrm{L}_2(Ra)\,\boldsymbol{x} = \dot{\boldsymbol{x}} + \begin{pmatrix} 4 & -4 & 0 \\ -1 & 1 & (Ra-1)^{1/2} \\ -(Ra-1)^{1/2} & k_p-(Ra-1)^{1/2} & 1 \end{pmatrix} \boldsymbol{x}$$

$$= \begin{pmatrix} 0 \\ -x_1 x_3 \\ x_1 x_2 - k_n x_2^3 \end{pmatrix}. \tag{8}$$

L_1 and L_2 are linear operators. Using a parametrization in terms of ϵ, we expand $\boldsymbol{x}$ and Ra into the power series

$$\boldsymbol{x} = \epsilon \boldsymbol{x}_1 + \epsilon^2 \boldsymbol{x}_2 + \epsilon^3 \boldsymbol{x}_3 + \cdots \text{c.c.} = \epsilon a(\tau_1, \tau_2)\, \boldsymbol{\zeta} \exp(\mathrm{i}\omega_0 t) + \epsilon^2 \boldsymbol{x}_2 + \epsilon^3 \boldsymbol{x}_3 + \cdots \text{c.c.} \tag{9}$$

and

$$Ra = Ra_H + \epsilon^2 R_2 + \cdots, \tag{10}$$

where $\tau_j = \epsilon^{2j} t$ are slow times and a is an amplitude function. $\boldsymbol{x}_j = \{x_{j,1}, x_{j,2}, x_{j,3}\}$. ϵ is defined by

$$[a\epsilon, 1] = [\boldsymbol{x}, \boldsymbol{\zeta}^* \,\mathrm{e}^{\mathrm{i}\omega_0 t}]. \tag{11}$$

The eigensystem $\{\mathrm{i}\omega_0, \boldsymbol{\zeta}\}$ satisfies the equation

$$\mathrm{L}_3 \boldsymbol{\zeta} = [\mathrm{i}w_0 I + \mathrm{L}_2(Ra_H)]\, \boldsymbol{\zeta} = 0, \tag{12}$$

where $Ra_H = 1 + \frac{1}{4}((60 + k_p^2)^{1/2} - k_p)^2$ and $\omega_0^2 = Ra_H + 4 - k_p(Ra_H - 1)^{1/2}$. Note that Ra_H increases (decreases) as the linear gain $-k_p$ (k_p) increases. Thus, the linear controller can be used to shift the Hopf bifurcation point at will. The feasibility of doing so has been confirmed experimentally in WSB.

In the above, $\langle \boldsymbol{\zeta}, \boldsymbol{\zeta}^* \rangle = \boldsymbol{\zeta} \cdot \overline{\boldsymbol{\zeta}^*} = 1$ and $\mathrm{L}_3^* \boldsymbol{\zeta}^* = 0$. The superscript * denotes the adjoint and the overbar denotes the complex conjugate. $\langle \boldsymbol{v}, \boldsymbol{w} \rangle = \boldsymbol{v} \cdot \overline{\boldsymbol{w}}$ and $[\boldsymbol{v}, \boldsymbol{w}] = \omega_0 / 2\pi \int_0^{2\pi/\omega_0} \langle \boldsymbol{v}, \boldsymbol{w} \rangle \,\mathrm{d}t$ are inner products.

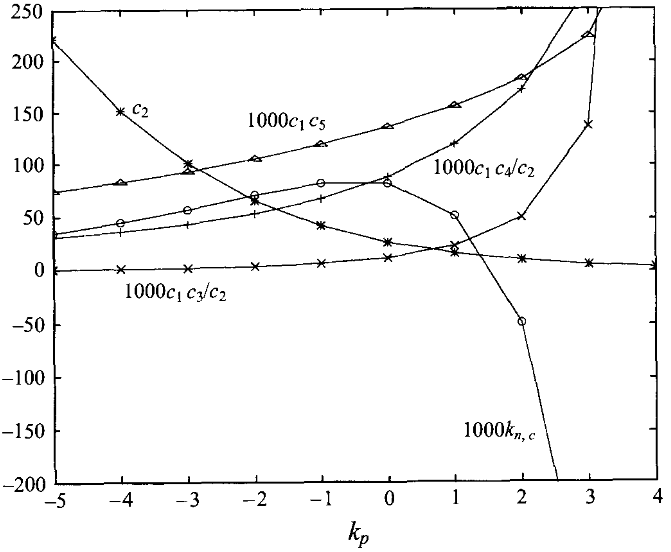

FIGURE 4. The magnitudes of the coefficients $k_{n,c}$, c_2, c_1c_3/c_2, c_1c_4/c_2 and c_1c_5 are depicted as functions of k_p.

Equation (12), the $O(\epsilon)$ equation, is the linear stability problem. At $O(\epsilon^3)$ and $O(\epsilon^3)$, we obtain, respectively,

$$\mathrm{L}_1(Ra_H)\,x_2 = \begin{pmatrix} 0 \\ -x_{1,1}x_{1,3} \\ x_{1,1}x_{1,2} \end{pmatrix} \tag{13}$$

and

$$\mathrm{L}_1(Ra_H)\,x_3 = -\frac{\partial x_1}{\partial \tau_1} + \frac{R_2}{2(Ra_H-1)^{1/2}} \begin{pmatrix} 0 \\ -x_{1,3} \\ x_{1,1}+x_{1,2} \end{pmatrix} + \begin{pmatrix} 0 \\ -x_{2,1}x_{1,3}-x_{1,1}x_{2,3} \\ x_{1,1}x_{2,2}+x_{2,1}x_{1,2} \end{pmatrix} - k_n \begin{pmatrix} 0 \\ 0 \\ x_{1,2}^3 \end{pmatrix}. \tag{14}$$

We solved equation (13) together with the normalization condition (11) to obtain x_2. Subsequently, we imposed a solvability condition on the right-hand side of (14) to obtain the equation

$$\frac{\partial a}{\partial \tau_1} = c_1\,a\{[c_2\,|a|^2(k_{n,c}+k_n)+R_2]+\mathrm{i}[-|a|^2(c_3+c_4k_n)+c_5R_2]\}, \tag{15}$$

where the coefficients $c_j(j=1,\dots,5)$ and $k_{n,c}$ are all functions of k_p. The numerical values of these coefficients depend on the particular choice of normalization for ζ. Here, we use

$$\zeta = \left\{1, \frac{4+\mathrm{i}\omega_0}{4}, A_1+\mathrm{i}A_2\right\}, \quad A_1 = \frac{(\omega_0^2+8)(Ra_H-1)^{1/2}-k_p\omega_0^2-4k_p}{4(\omega_0^2+1)},$$

$$A_2 = \frac{\omega_0(3k_p-7(Ra_H-1)^{1/2})}{4(\omega_0^2+1)}.$$

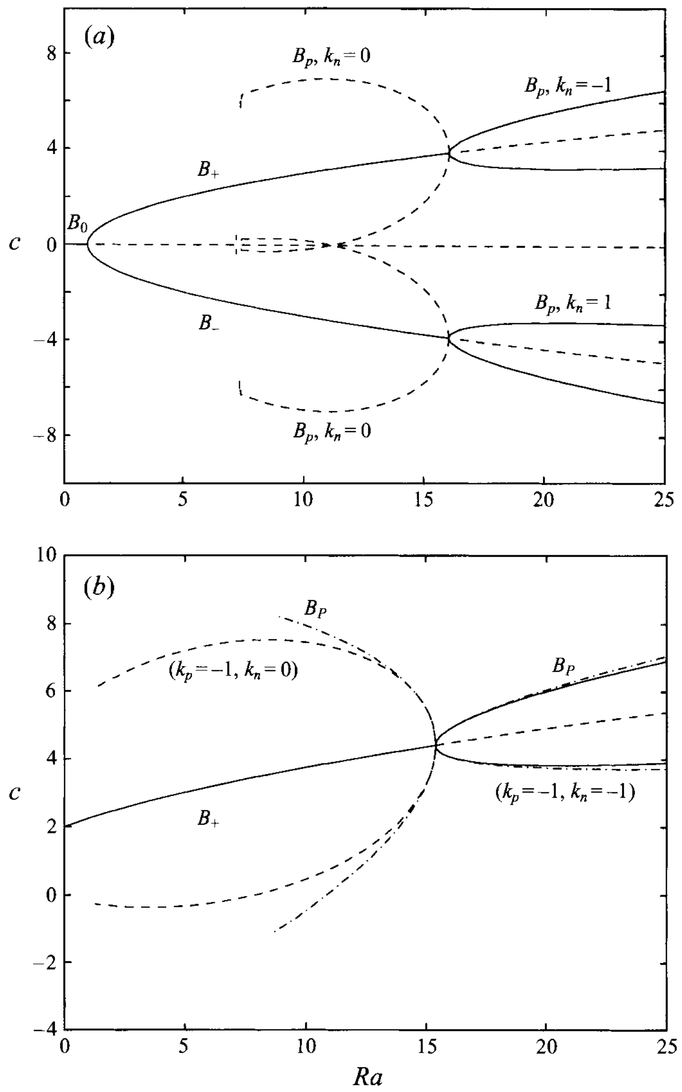

FIGURE 5. The states B_+ and B_p are depicted as functions of *Ra* for $k_n = 0$ and $k_n = -1$ and $P = 4$. (*a*) $k_p = 0$, (*b*) $k_p = -1$. The solid and dashed lines correspond, respectively, to linearly stable and nonstable numerical solutions. The dash–dot lines in (*b*) represent the analytic solutions.

The coefficients c_j were computed symbolically using Macsyma 417.125 (delta 2) (1993). Owing to their considerable length, they are not presented here. For further details, the interested reader is referred to Yuen (1997).

From (15), we obtain the amplitude equation

$$\frac{\partial |a|^2}{\partial \tau_1} = 2c_1 |a|^2 [c_2 |a|^2 (k_{n,c} + k_n) + R_2]. \tag{16}$$

When $(k_{n,c} + k_n) \gg \epsilon$, the amplitude of the bifurcating periodic solution, B_P, is

$$|a|^2 = -\frac{R_2}{c_2(k_{n,c} + k_n)}. \tag{17}$$

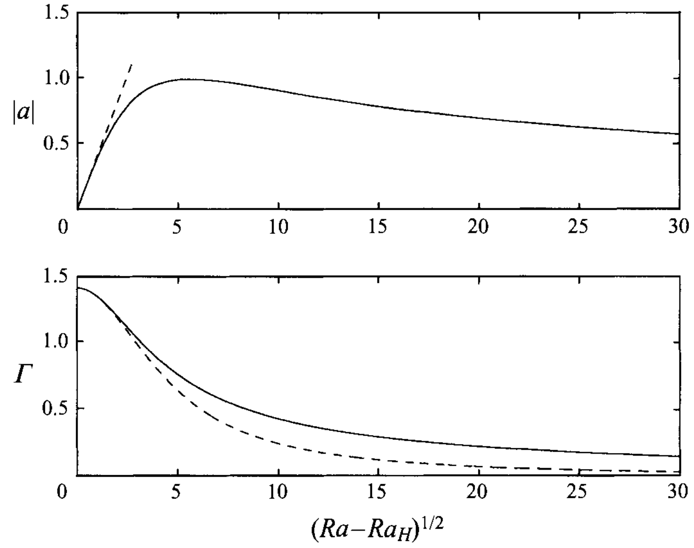

FIGURE 6. The amplitude, $|a|$, and the period $\Gamma = 2\pi/\omega$, are depicted as functions of Ra for $k_n = -1$ and $k_p = 0$. $P = 4$. The solid and dashed lines correspond, respectively, to numerical and analytical solutions.

Equation (17) is not valid when $k_{n,c} + k_n = O(\epsilon)$ since then a is no longer $O(1)$ and the series (9) is not uniformly valid.

When we shift the Hopf bifurcation point upwards ($k_p < 0$), c_1, c_2 and $k_{n,c}$ are always positive. For example, when $k_p = 0$, $c_1 = 1/56$, $c_2 = 27\sqrt{15}/4$, and $k_{n,c} = 248/(783\sqrt{15})$. The values of c_2 and $k_{n,c}$ as functions of k_p are depicted in figure 4. When $k_n > -k_{n,c}$, the bifurcation is subcritical and the periodic orbit (17) is non-stable. By selecting a nonlinear controller gain, $k_n < -k_{n,c}$, one would render the subcritical bifurcation supercritical and the periodic orbit (17) stable.

The frequency of the bifurcating solution, $a = |a|\,e^{i\omega_2\tau_1}$, is $\omega = \omega_0 + \epsilon^2\omega_2$, where

$$\omega_2 = c_1 R_2\left[-\frac{(c_3 + c_4 k_n)}{c_2(k_{n,c} + k_n)} + c_5\right]. \tag{18}$$

The values of $c_1 c_3/c_2, c_1 c_4/c_2$ and $c_1 c_5$ as functions of k_p are depicted in figure 4.

2.5. *Numerical solutions*

With the aid of the bifurcation software AUTO (Doedel 1986) we computed the periodic orbits (equations (4)–(7)) numerically. Figures 5(*a*) and 5(*b*) depict the bifurcation diagrams for $k_p = 0$ and $k_p = -1$, respectively. In each figure, results are shown for $k_n = 0$ and -1. Figure 5(*b*) also depicts the analytical results of §2.4 for B_P (dash–dot lines). Note the good agreement between the analytical and numerical results in the vicinity of the bifurcation point ($Ra = Ra_H$). The solid and dashed lines represent, respectively, stable and non-stable solution branches. When $k_n = 0$ (-1), the Hopf bifurcation is subcritical (supercritical). As k_p decreases from zero (figure 5*a*) to -1 (figure 5*b*), the Hopf bifurcation is delayed from 16 to ~ 20.4. Figures 5(*a*) and 5(*b*) illustrate that the nonlinear controller can invert the direction of the bifurcation.

The numerical (solid lines) and analytical (dashed lines) results are further compared in figure 6 for $k_p = 0$ and $k_n = -1$. The figure depicts the amplitude, $|a|$, and the period, $\Gamma = 2\pi/\omega$, as functions of $(Ra - Ra_H)^{1/2}$. For $(Ra - Ra_H)^{1/2} < 2$, there is excellent agreement between the analytical and numerical results. As $(Ra-Ra_H)^{1/2}$ increases, the amplitude of B_P initially increases and then decreases. The period decreases monotonically as $(Ra-Ra_H)^{1/2}$ increases.

The theoretical study illustrates that through the use of nonlinear control, one can render the subcritical bifurcation supercritical, replace a chaotic strange attractor with a periodic one, and eliminate the hysteresis phenomenon. In the next section, we will demonstrate that some of these theoretical predictions can be verified in an experiment.

3. Experiments

In this section, we first describe the experimental apparatus. Then, we show that the control strategy described in §2.3 can actually be used in practice.

3.1. *The experimental apparatus*

The apparatus we used here is somewhat different than the one we used in WSB, which was destroyed when it was used in our undergraduate laboratory. Therefore, some of the observations reported here may differ slightly from the ones described in WSB.

The apparatus (figure 1) consists of a Pyrex pipe of diameter d (= 0.030 m) bent into a torus of diameter D (= 0.760 m). It stands in the vertical plane. The lower half of the apparatus is heated with a uniform-heat-flux resistance heater while the upper half is submerged in a jacket containing a flowing coolant. The flow dynamics depend sensitively on the coolant's temperature. Hence, the coolant was supplied by a constant-temperature bath at a temperature of 25 ± 1 °C, and it was circulated at a sufficiently high flow rate to approximate a uniform wall temperature. The heater consists of a metallic layer (instatherm) coated directly onto the glass tube. This arrangement assures low thermal resistance between the glass tube and the heater. The heater is well insulated to minimize heat losses to the ambient. The power supply to the heater is computer-controlled. During the experiments, the ambient temperature was 24 ± 2 °C.

In our experiments, we measured the total heat input to the heater (Q), the coolant's temperature, and the fluid (water) temperature differences between positions 3 and 9 o'clock and between positions 6 and 12 o'clock around the loop which we denoted as ΔT_{3-9} and ΔT_{6-12}, respectively. All quantities were continuously monitored as functions of time with the aid of a computer-controlled data acquisition system. The direction of the flow in the loop and, to some extent, the velocity profile could be directly observed due to the presence of small particles in the liquid.

3.2. *The uncontrolled flow in the loop*

Below, we briefly describe the various flow regimes observed in the loop as a function of the input heating rate in the absence of a controller. When heating and cooling were applied to the isothermal loop, depending on (stochastic) initial conditions and the loop imperfections, the fluid motion occurred either in the counterclockwise or clockwise direction. For relatively low heating rates, the flow inside the loop experienced low-amplitude oscillations and it was unidirectional. Figure 7 depicts $c \sim \Delta T_{3-9}$ as a function of time, prior to the onset of chaos. $Q = 90$ W $\sim 0.9Q_C$, where Q_C denotes the power setting at which chaotic behaviour was first observed. The temperature data were sampled at a rate of 0.2 Hz.

The power spectrum of ΔT_{3-9} (figure 7) is depicted in figure 8(a). We quantified the magnitude of the temperature oscillations by computing the signal r.m.s., r.m.s. = $(1/N\sum_{t=1}^{N}[\Delta T_{3-9}(t)-\overline{\Delta T_{3-9}}]^2)^{1/2}$, where $\overline{\Delta T_{3-9}} = (1/N)\sum_{t=1}^{N}|\Delta T_{3-9}(t)|$ and $N = 1000$. The

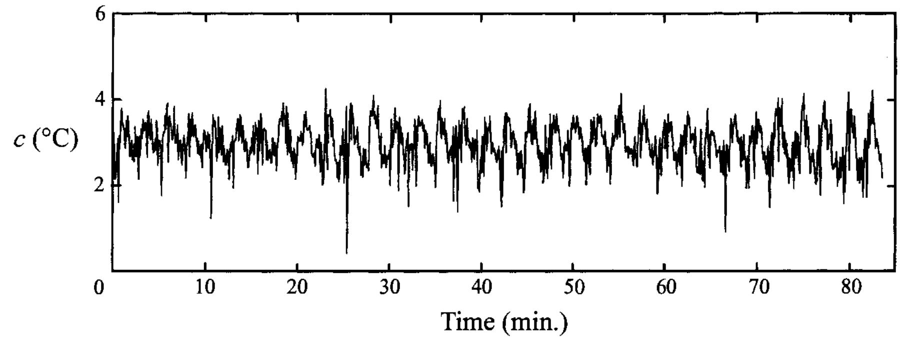

FIGURE 7. The experimentally measured temperature difference between positions 3 and 9 o'clock is depicted as a function of time for $Q = 90$ W $= 0.9Q_C$.

r.m.s. of the oscillations was about 17% of the mean value of ΔT_{3-9}. Although the signal depicted in figure 7 has a time-dependent component, we assume that it describes the state B_+. We speculate that the low-amplitude oscillations were caused by noise in the system, by the local instabilities induced, for example, when the hot fluid exited from the heated (cooled) section into the cooled (heated) one, and by the presence of the non-stable periodic orbit generated at the subcritical bifurcation. Although the periodic orbit is non-attracting, it can still influence the transient behaviour of the system.

When the heating rate exceeded the critical value, Q_C, the flow became oscillatory and time-dependent with occasional reversals in direction. The critical heating rate Q_C depended on the coolant and room temperatures. When the coolant temperature was 25 °C, $Q_C = 100 \pm 5$ W. Figure 2 depicts $c \sim \Delta T_{3-9}$ as a function of time in the chaotic regime. $Q = 330$ $W \sim 3.3Q_C$. Witness the irregular oscillations and the occasional changes in the sign of c. These changes in sign correspond to changes in the direction of the flow. The fluid spent roughly 63% of the time flowing in the counterclockwise direction and 37% in the clockwise direction. The apparent bias in favour of the counterclockwise direction conceivably may be attributable to insufficient data and/or a small asymmetry in the apparatus.

The power spectrum of the signal from figure 2 is depicted in figure 8(*b*). There are no dominating frequencies in the power spectrum. Figure 9 depicts a three-dimensional portrait of the attractor constructed from the ΔT_{3-9} time series (figure 2) using the time delay technique and a three-dimensional embedding space. The time delay used in the construction was 10 s. The data were filtered using a Butterworth low-pass filter with cut-off and rejection frequencies of 0.015 and 0.02 Hz, respectively. The passband and stopband attenuations for the filter were, respectively, 3 and 15 dB. The experimental phase-space portrait in figure 9 resembles the well-known phase portrait (not shown here) of the Lorenz (1963) attractor which can be obtained by integrating equations (4)–(6) with $W_1 = -1$. In the region $Q > Q_C$, the flow closely resembles the chaotic motion, B_C, predicted by the theoretical model (§2.2).

We carried out a sequence of experiments to detect the presence of a hysteresis phenomenon. In one set of experiments, we started at a power setting $Q < Q_C$, and we gradually increased Q until chaotic flow was observed. We marked the power at which the transition from unidirectional to chaotic flow occurred as Q_C^-. Subsequently, we started the experiment in the chaotic regime and gradually decreased Q until unidirectional flow was observed. We marked the transition point from chaotic to unidirectional flow as Q_C^+. Within our experimental precision, no significant differences

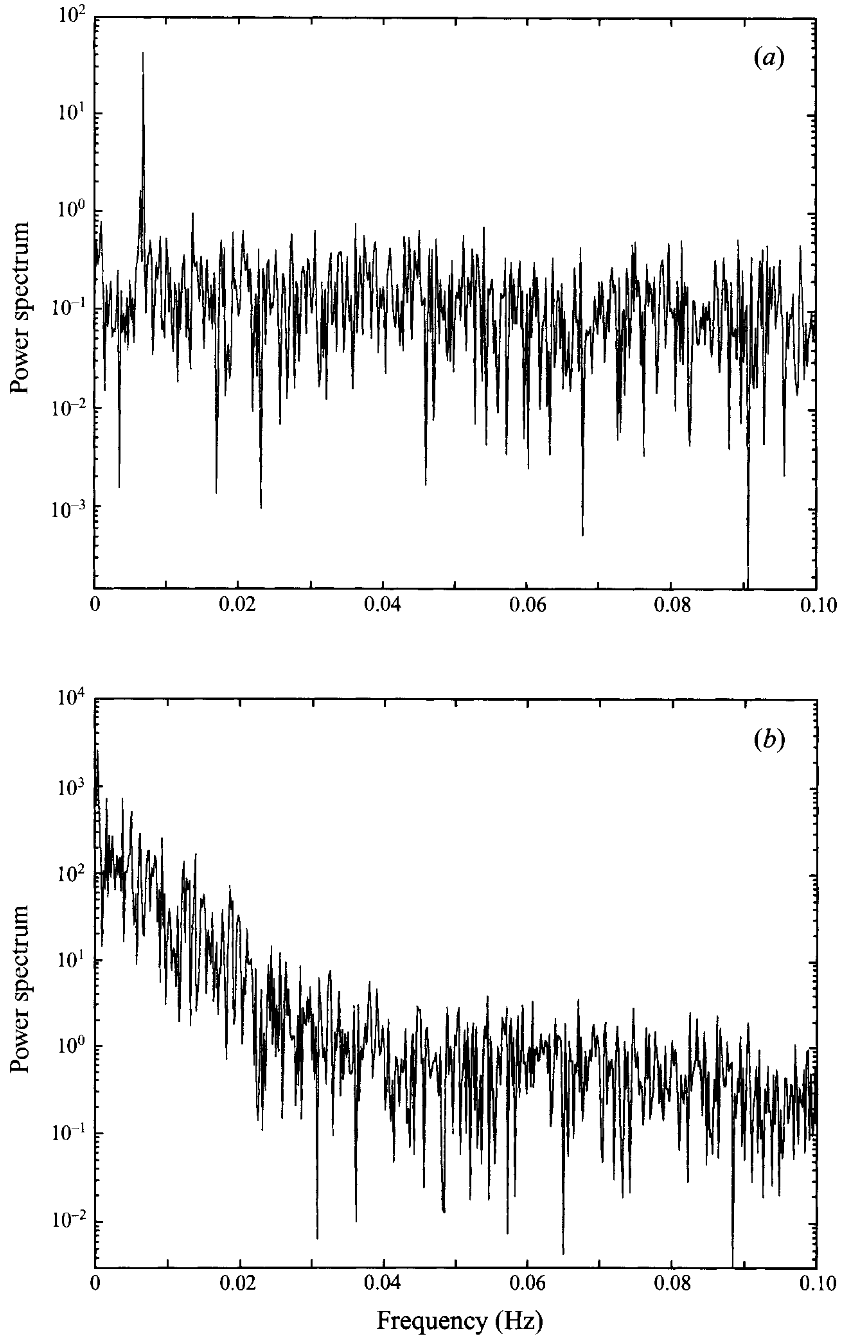

FIGURE 8. The power spectrum of the experimentally measured temperature difference between positions 3 and 9 o'clock: (*a*) as depicted in figure 7. $Q = 90\ \mathrm{W} = 0.9Q_C$; (*b*) as depicted in figure 2. $Q = 330\ \mathrm{W} = 3.3Q_C$.

were detected between Q_C^+ and Q_C^-. This is consistent with the mathematical model which predicts a very narrow hysteresis region. Because of the lack of a significant size of hysteresis interval, we were not able to demonstrate the effect of the nonlinear controller on the hysteresis phenomenon.

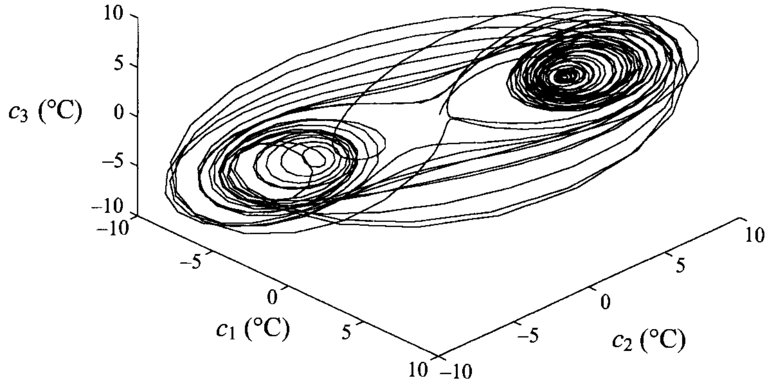

FIGURE 9. The attractor is reconstructed, using the time delay technique (with a time delay of 10 s), in a three-dimensional embedding space from the time series depicted in figure 2. $Q = 330\ \mathrm{W} = 3Q_C$.

3.3. *The controlled system*

The theoretical investigation presented in §2 suggests that the characteristics of the motion can be modified considerably with the use of a controller. In this section, we wish to demonstrate that these ideas can be used in practice. In WSB, we used linear control to make the flow approximately steady while operating at power levels which nominally yielded chaotic motion. In other words, we postponed the transition to chaos and increased the magnitude of Q_C. Here, we wish to examine the effect of the nonlinear controller on the flow dynamics and demonstrate that we can replace the chaotic attractor (B_C) with a periodic one (B_P).

To accomplish this objective, we used two different control strategies. In one control strategy, we used ΔT_{3-9} as the control input and in the other ΔT_{6-12} was the control input. The first control strategy is the one analysed in §2.3 and it will be discussed first. We denote the temperature difference which corresponds to state B_+ by $\overline{\Delta T_{3-9}}$. Next, we argue that the steady solution, albeit non-stable, still exists in the chaotic regime ($Q > Q_C$), where ΔT_{3-9} is now time-dependent. We wish to modify the heat input to the loop in proportion to the deviations of ΔT_{3-9} from $\overline{\Delta T_{3-9}}$. To this end, we set the control rule:

$$Q(t-t_d) = Q_0 + k_p[\Delta T_{3-9}(t) - \overline{\Delta T_{3-9}}] + k_n[\Delta T_{3-9}(t) - \overline{\Delta T_{3-9}}]^3. \qquad (19)$$

In the second instance, we replaced ΔT_{3-9} with ΔT_{6-12} in (19). Since the theory for this second control strategy is similar to the one presented in §2.3, we did not repeat the theoretical derivation for the second case.

In (19), t_d denotes the time delay associated with the heater's response. By experimenting with various time delays, we identified $t_d \sim 15$ s as providing the most satisfactory results. The application of the control at time t required a prediction of the signal at time $t + t_d$. The predicted signals ΔT_{3-9} (ΔT_{6-12}) used in (19) were obtained by extrapolating the measured data. This was done by storing in the memory ΔT_{3-9} (ΔT_{6-12}) at times t, $t-5$ s, $t-10$ s, $t-15$ s and $t-20$ s. Least-squares regression was used to fit the data with a curve of the form $\Delta T_{3-9} = a_0 + a_1 t + a_2 t^2$. This quadratic expression was used to predict ΔT_{3-9} (ΔT_{6-12}) at time $t + t_d$. Before activating the controller, the magnitude of $\overline{\Delta T_{3-9}}$ (ΔT_{6-12}) was estimated by time-averaging $|\Delta T_{3-9}|$ (ΔT_{6-12}) over a time interval of 5000 s. After activating the controller, this average was continuously modified every 300 s during the course of the experiment.

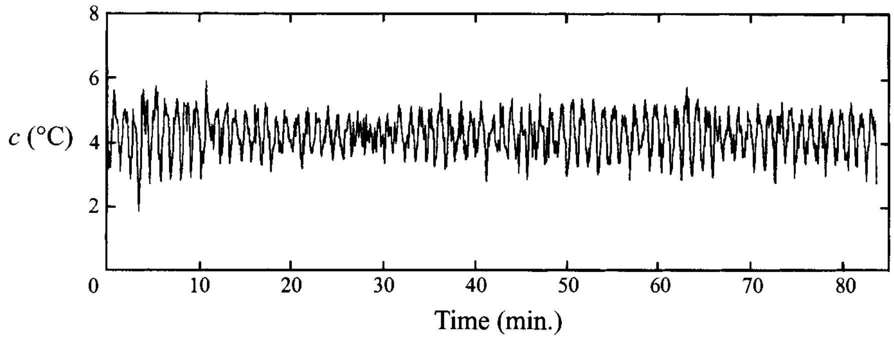

FIGURE 10. The controlled, experimentally measured temperature difference between positions 3 and 9 o'clock is depicted as a function of time for $Q_0 = 330$ W $= 3.3Q_C$, $k_p = 0$, $k_n = -1.2$ W °C^{-3} and $t_d = 15$ s.

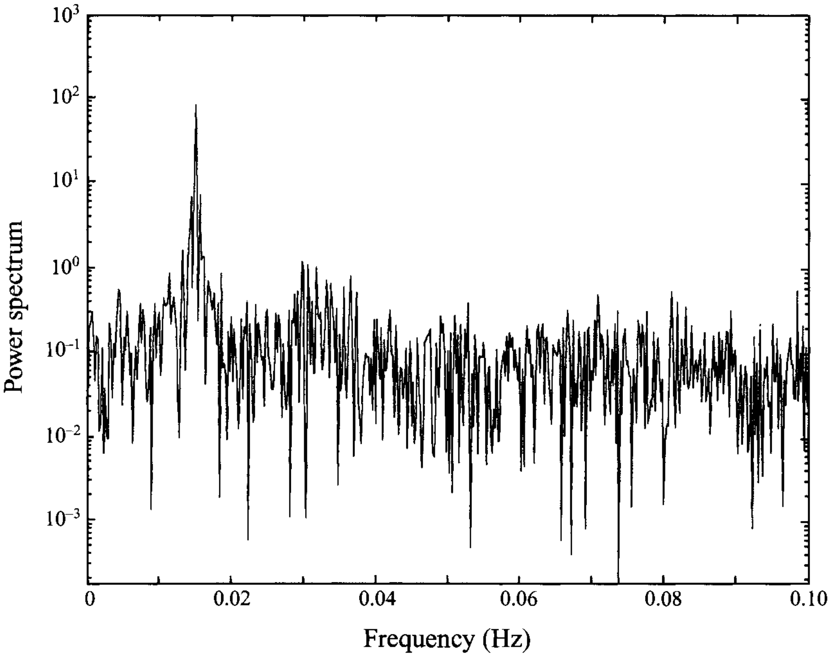

FIGURE 11. The power spectrum of the controlled, experimentally measured temperature difference between positions 3 and 9 o'clock depicted in figure 10.

3.3.1. $\Delta T_{3\text{-}9}$ *control*

The results of the control strategy (19) with $\Delta T_{3\text{-}9}$ as the observed signal are shown in figure 10. The figure depicts $c \sim \Delta T_{3\text{-}9}$ as a function of time for $Q_0 = 330$ W $= 3.3Q_C$ and controller gains $k_p = 0$ and $k_n = -1.2$ W °C^{-3}. Figure 10 should be contrasted with figure 2. The controller replaced the chaotic attractor with occasional reversals in the flow direction (figure 2) with an almost periodic attractor and with unidirectional flow. The r.m.s. of the oscillations in figure 10 was about 15% of the averaged signal.

The power spectrum of the signal of figure 10 is depicted in figure 11. The power spectrum exhibits a relatively strong periodic component at frequency ~ 0.015 Hz. Figure 11 should be contrasted with the power spectrum in the absence of the controller (figure 8(*b*)). In contrast to WSB, here we are stabilizing a periodic orbit. Therefore, when the nonlinear controller is active, the heating rate is a function of time.

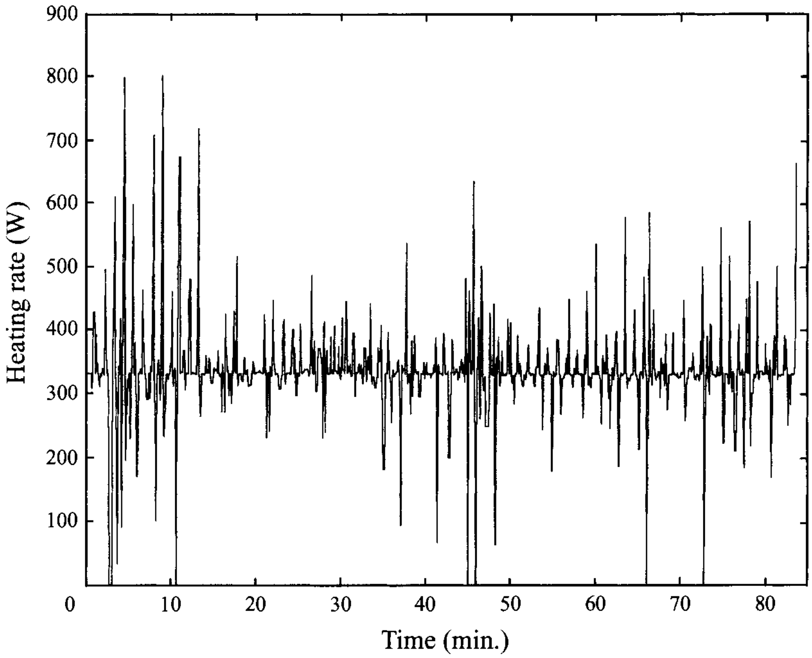

FIGURE 12. The controlled, experimentally measured heating rate as a function of time for the case shown in figure 10.

The power supplied to the heater as a function of time is depicted in figure 12. Most of the time, the fluctuations in the power were relatively small. Occasionally, however, the controller required high-amplitude power oscillations which sometimes exceeded the operational limits of the power supply. In other words, the controller occasionally saturated.

Next, we examined the amplitude of the periodic limit cycle as a function of the power input. Using open circles, figures 13(*a*) and 13(*b*) depict the experimentally measured $\overline{\text{r.m.s.}/\Delta T_{3\text{-}9}}$ and Γ/Γ_H as functions of the normalized power input Q/Q_C for $k_p = 0$ and $k_n = -1.2$ W °C^{-3}. The period Γ_H corresponds to the dominant frequency when $Q \sim Q_C$. The theoretical results $|a|/(Ra-1)^{1/2}$ and $\Gamma/\Gamma_H(k_p = 0, k_n = -1)$ are shown as solid curves in figure 13. In the theoretical model, as Ra increases above Ra_H, the relative amplitude of the periodic orbit increases, achieves a maximum, and then decreases. In contrast, as Q/Q_C increases, $\overline{\text{r.m.s.}/\Delta T_{3\text{-}9}}$ initially decreases, attains a minimum, and then slightly increases. Both the theoretically predicted and experimentally measured periods decrease monotonically as Ra increases (figure 13*b*). There is good agreement between the theoretically predicted period and the experimentally observed one.

The discrepancies between the experimental observations and the theoretical predictions can be attributed to the mathematical model being too simple to provide an accurate quantitative description of the dynamics of our loop and to inaccurate estimation of various experimental variables such as the loop's Prandtl number, the time delay, t_d, and the magnitude of $\overline{\Delta T_{3\text{-}9}}$ corresponding to the non-stable B_+ branch. Moreover, as the power input varied, both P and t_d changed as well. These variations in P and t_d were not accounted for in either the experimental controller or the theory. Finally, in the experiment, the flow was subject to local instabilities resulting from the hot (cold) fluid entering the cold (hot) section of the loop at locations 3 and 9 o'clock.

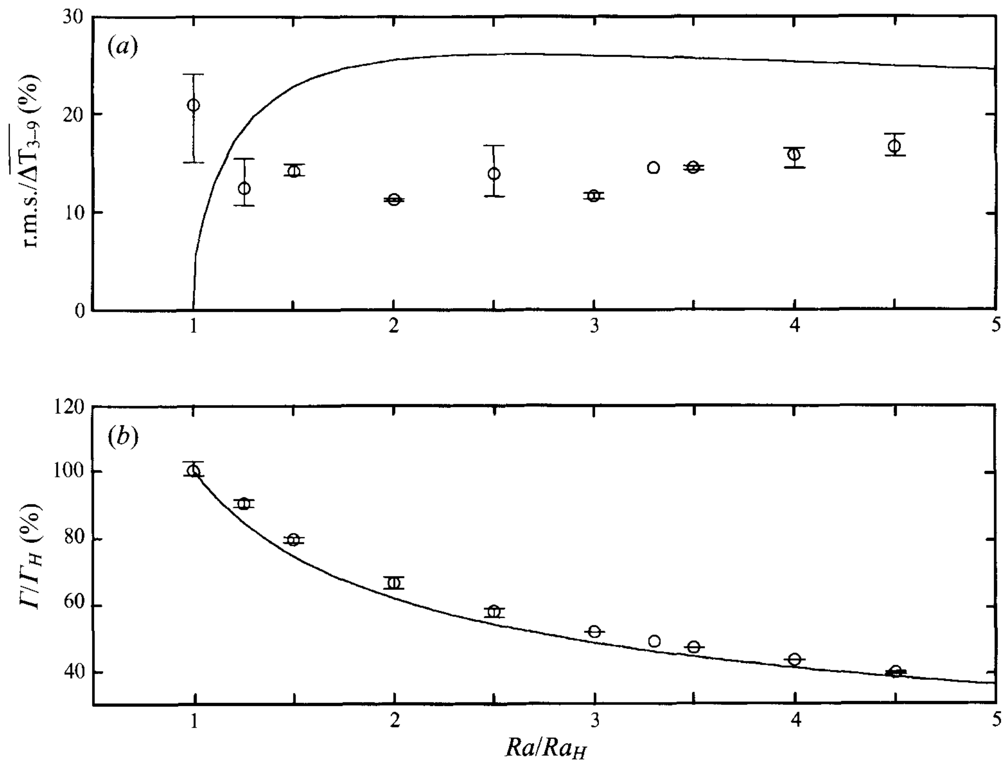

FIGURE 13. R.m.s./$\overline{\Delta T_{3-9}}$ and Γ/Γ_H are depicted as functions of Ra/Ra_H for $k_p = 0$, $P = 4$. The solid lines ($k_n = -1$) and hollow circles ($k_n = -1.2$ W °C^{-3}) with estimated errors (I-bars) correspond, respectively, to numerical and experimental results.

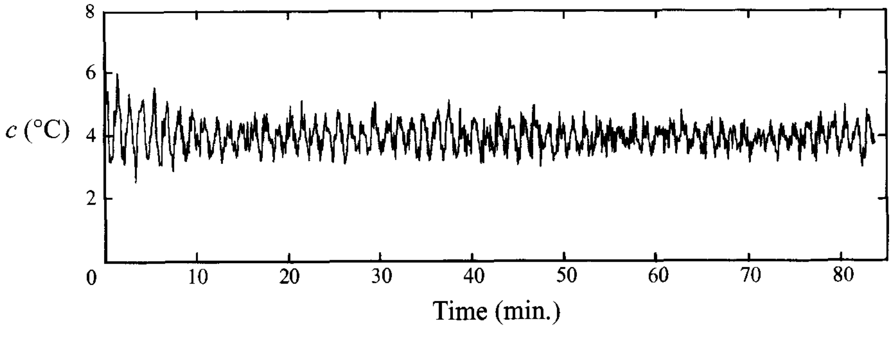

FIGURE 14. The controlled, experimentally measured temperature difference between positions 3 and 9 o'clock is depicted as a function of time for $Q_0 = 250$ W $= 2.5Q_C$, $k_p = 0$, $k_n = -1.2$ W °C^{-3} and $t_d = 15$ s.

These local instabilities were not accounted for in the mathematical model. In addition to affecting the global dynamics, these instabilities caused relatively high-frequency oscillations in the signal ΔT_{3-9}. Since the temperature measurements at locations 6 and 12 o'clock were less sensitive to these local instabilities, we decided to test the performance of the controller using the signal ΔT_{6-12} as the control signal instead of ΔT_{3-9}.

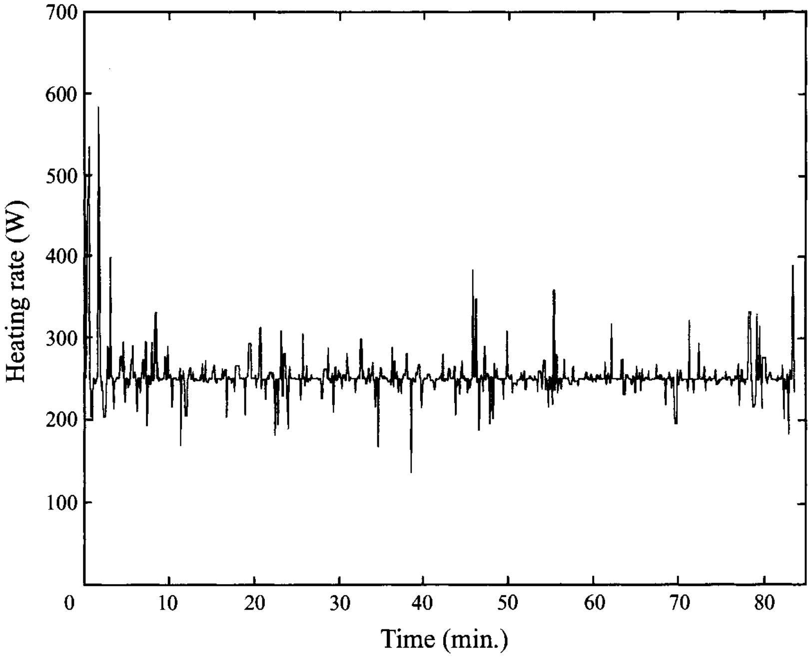

FIGURE 15. The controlled, experimentally measured heating rate as a function of time for the case shown in figure 14.

3.3.2. ΔT_{6-12} *control*

We used the same control strategy as described in equation (19) with ΔT_{6-12} replacing ΔT_{3-9}. Since ΔT_{6-12} is the same for both B_+ and B_-, a ΔT_{6-12}-based controller will not discriminate between these two solution branches. Depending on initial conditions, it will stabilize a periodic orbit with the time-averaged flow going either in the counterclockwise or the clockwise directions.

Figures 14 and 15 depict $c \sim \Delta T_{3-9}$ and the power input to the loop as functions of time for $Q_0 = 250$ W $= 2.5Q_C$ and controller gains $k_p = 0$ and $k_n = -1.2$ W °C^{-3}. The r.m.s. of the oscillations in figure 14 was 10% of the averaged signal. Clearly, the nonlinear controller has successfully replaced the chaotic motion with an almost periodic one. Figure 15 illustrates that when the ΔT_{6-12} type control is used, the power oscillations are much smaller than when the ΔT_{3-9} type control is used (figure 12). This reduction in the power oscillations is a result of the ΔT_{6-12} signal being less noisy than the ΔT_{3-9} signal.

4. Discussion and conclusions

In this paper, we have demonstrated theoretically and experimentally that a nonlinear controller can be used to render a subcritical Hopf bifurcation supercritical. To illustrate how the controller operates, we briefly describe the mechanism responsible for the chaotic, oscillatory behaviour of the flow in the loop (Welander 1967). To this end, imagine that a small disturbance causes the flow to slow down to below the steady-state flow rate. As a result, the fluid spends more time in the heater (cooler) section, gains (loses) more heat than usual, and emerges from the heater (cooler) with a temperature higher (lower) than usual. This, in turn, causes an increase in the buoyancy force with a corresponding increase in the fluid velocity. Once the fluid velocity increases, the process reverses itself. Under appropriate conditions, these oscillations amplify and, in the uncontrolled system, eventually lead to the chaotic behaviour depicted in figure 2. In contrast, when the controller is operating, it detects the appearance of disturbances by monitoring deviations in the temperature difference $\Delta T_{3-9} - \overline{\Delta T_{3-9}}$ or $\Delta T_{6-12} - \overline{\Delta T_{6-12}}$. Once a deviation is detected, the controller takes action to counteract its effect. For instance, if the deviation tends to accelerate (decelerate) the flow, the heating rate is increased (decreased) to counteract this effect. Thus, a linear controller succeeds in taming chaos and replacing the chaotic flow with a time-independent flow. The nonlinear controller's effect is significant only when the disturbances grow to a considerable amplitude. As a result, the nonlinear controller cannot stabilize the B_+ state, but rather replaces it with a periodic state.

Both in experiment and theory, the nonlinear controller was successful in replacing the naturally occurring chaotic motion with a periodic one. The results of this work suggest that the nonlinear control can be used to render subcritical bifurcations supercritical and thus increase the domain of attraction of the stabilized state and perhaps eliminate early loss of stability through by-pass mechanisms. The challenge now is to apply control strategies to more complicated flow phenomena such as planar Poiseuille and boundary layer flows.

REFERENCES

ABED, E. H. & FU, J. H. 1986 Local feedback stabilization and bifurcation control. I – Hopf bifurcation. *Systems Control Lett.* **7**, 11–17.

BAU, H. H. & TORRANCE, K. E. 1981 Transient and steady behavior of an open, symmetrically-heated, free convection loop. *Int J. Heat Mass Transfer* **24**, 597–609.

BAU, H. H. & WANG, Y.-Z. 1991 Chaos: a heat transfer perspective. *Ann Rev Heat Transfer*, IV, (C. L. Tien, editor), 1–50, Hemisphere.

CHEN, T. S. & JOSEPH, D. D. 1973 Subcritical bifurcation of plane Poiseuille flow. *J. Fluid Mech.* **58**, 337–351.

CREVELING, H. F., DE PAZ, J. F., BALADI, J. Y. & SCHOENHALS, R. J. 1975 Stability characteristics of a single phase thermal convection loop. *J. Fluid Mech.* **67**, 65–84.

DOEDEL, E. 1986 *AUTO: Software for Continuation and Bifurcation Problems in Ordinary Differential Equations.* Applied Mathematics Report, California Institute of Technology.

EHRHARD, P. & MULLER, U. 1990 Dynamical behaviour of natural convection in a single-phase loop. *J. Fluid Mech.* **217**, 487–518.

GORMAN, M., WIDMANN, P. J. & ROBINS, K. A. 1984 Chaotic flow regimes in a convection loop. *Phys. Rev. Lett.* **52**, 2241–2244.

GORMAN, M., WIDMANN, P. J. & ROBINS, K. A. 1986 Nonlinear dynamics of a convection loop: a quantitative comparison of experiment with theory. *Physica* **19D**, 255–267.

HART, J. E. 1984 A new analysis of the closed loop thermosyphon. *Intl J. Heat Mass Transfer* **27**, 125–136.

HART, J. E. 1985 A note on the loop thermosyphon with mixed boundary conditions. *Intl J. Heat Mass Transfer* **28**, 939–947.

HU, H. H. & BAU, H. H. 1994 Feedback control to delay or advance linear loss of stability in planar Poiseuille flow. *Proc. R. Soc. Lond.* A **447**, 299–312.

LORENZ, E. N. 1963 Deterministic nonperiodic flow. *J. Atmos. Sci.* **20**, 130–141.

MALKUS, W. V. R. 1972 Non-periodic convection at high and low Prandtl number. *Mem. Soc. R. Sci. Liege* (6) IV, 125–128.

ROBBINS, K. A. 1977 A new approach to subcritical instability and turbulent transitions in a simple dynamo. *Math. Proc. Camb. Phil. Soc.* **82**, 309–325.

SINGER, J. & BAU, H. H. 1991 Active control of convection. *Phys. Fluids* A **3**, 2859–2865.

SINGER, J., WANG, Y.-Z. & BAU, H. H. 1991 Controlling a chaotic system. *Phys. Rev. Lett.* **66**, 1123–1126.

SPARROW, C. 1982 *The Lorenz Equations: Bifurcations, Chaos, and Strange Attractors.* Springer.

TANG, J. & BAU, H. H. 1993*a* Stabilization of the no-motion state in Rayleigh–Bénard convection through the use of feedback control. *Phys. Rev. Lett.* **70**, 1795–1798.

TANG, J. & BAU, H. H. 1993*b* Feedback control stabilization of the no-motion state of a fluid confined in a horizontal, porous layer heated from below. *J. Fluid Mech.* **257**, 485–505.

TANG, J. & BAU, H. H. 1994 Stabilization of the no-motion state in the Rayleigh–Bénard problem. *Proc. R. Soc. Lond.* A **447**, 587–607.

WANG, Y.-Z., SINGER, J. & BAU, H. H. 1992 Controlling chaos in a thermal convection loop. *J. Fluid Mech.* **237**, 479–498 (referred to herein as WSB).

WELANDER, P. 1967 On oscillatory instability of differentially heated fluid loop. *J. Fluid Mech.* **29**, 17–30.

WIDMANN, P. J., GORMAN, M. & ROBINS, K. A. 1989 Nonlinear dynamics of a convection loop II: chaos in laminar and turbulent flows. *Physica* D **36**, 157–166.

YORKE, A., YORKE, E. D. & MALLET-PARET, J. 1987 Lorenz-like chaos in partial differential equations. *Physica* **24D**, 279–291.

YUEN, P. 1997 Dynamics and control of flow in a thermal convection loop. PhD thesis, University of Pennsylvania.